

Journal of Materials Chemistry A

Accepted Manuscript



This is an *Accepted Manuscript*, which has been through the Royal Society of Chemistry peer review process and has been accepted for publication.

Accepted Manuscripts are published online shortly after acceptance, before technical editing, formatting and proof reading. Using this free service, authors can make their results available to the community, in citable form, before we publish the edited article. We will replace this *Accepted Manuscript* with the edited and formatted *Advance Article* as soon as it is available.

You can find more information about *Accepted Manuscripts* in the [Information for Authors](#).

Please note that technical editing may introduce minor changes to the text and/or graphics, which may alter content. The journal's standard [Terms & Conditions](#) and the [Ethical guidelines](#) still apply. In no event shall the Royal Society of Chemistry be held responsible for any errors or omissions in this *Accepted Manuscript* or any consequences arising from the use of any information it contains.

Cite this: DOI: 10.1039/c0xx00000x

ARTICLE TYPE

www.rsc.org/xxxxxx

The synergistic effects of Al and Te on the structure and Li⁺-mobility of the garnet-type solid electrolytes

Dawei Wang^a, Guiming Zhong^a, Oleksandr Dolotko^b, Yixiao Li^a, Matthew J McDonald^a, Jinxiao Mi^c, Riqiang Fu^d, Yong Yang^{*a}

⁵ Received (in XXX, XXX) Xth XXXXXXXXXX 20XX, Accepted Xth XXXXXXXXXX 20XX

DOI: 10.1039/b000000x

Abstract: The cubic garnet-type solid electrolyte Li₇La₃Zr₂O₁₂ with aliovalent doping exhibits a high ionic conductivity. However, the synergistic effects of aliovalent co-doping on the ionic conductivity of garnet-type electrolytes has rarely been examined. In this work, the synergistic effects of co-dopants Al and Te on the ionic conductivity of garnets were investigated using X-ray Diffraction (XRD), ²⁷Al/⁶Li Magic Angle Spinning Nuclear Magnetic Resonance (MAS NMR), Energy Dispersive X-ray Spectroscopy (EDS), Neutron Powder Diffraction (NPD) and Alternating Current (AC) impedance measurements. It was shown that co-dopants Al and Te stabilized the cubic lattice of Li_{7-2x-3y}Al_yLa₃Zr₂-xTe_xO₁₂ with specific Al/Te ratios, where additional Al had to be included in the structure if the amount of doped Te content *x* was below 0.5. In the Al and Te co-doped crystal structure, Al was incorporated in the tetrahedral 24*d* sites of lithium and Te occupied 16*a* sites of Zr. It was revealed that the occupancy of the latter could suppress the insertion of Al. High-resolution ⁶Li MAS NMR was able to differentiate the two lithium sites of interest in the garnet structure. Furthermore, it was shown that the mobility of Li ions at 24*d* sites mainly determined the bulk conductivities of the garnet-type electrolytes.

20 Introduction

Inorganic solid electrolytes have attracted more and more interest as a possible component of next generation batteries such as all-solid-state rechargeable Li (ion) batteries. Replacing liquid organic electrolytes by non-flammable, inorganic solid electrolytes is considered a potential solution^{1,2} to the safety issues encountered in conventional lithium ion batteries where dangerous liquid organic electrolytes are used. In particular, oxides with a garnet-type structure and a compound stoichiometry of A₃B₂C₃O₁₂ have attracted wide interest in recent years. Examples include Li₅La₃Nb₂O₁₂ and Li₇La₃Zr₂O₁₂, which exhibit an ionic conductivity of about 10⁻⁶ ~ 10⁻⁴ S cm⁻¹ at room temperature (RT)^{3,4}.

Li₅La₃Nb₂O₁₂ was first reported by Thangadurai *et al.* as a solid electrolyte with an ionic conductivity of 8 × 10⁻⁶ S cm⁻¹ at RT³, which was similar to that of its counterparts such as perovskite-type solid electrolytes⁵ and LISICONs⁶. However, another cubic garnet, Li₃Ln₃Te₂O₁₂, showed a negligible ionic conductivity at RT⁷. The primary difference in the ionic conductivities between Li₅La₃Nb₂O₁₂ and Li₃Ln₃Te₂O₁₂ was believed to be the lithium occupancy of distorted octahedral sites in Li₅La₃Nb₂O₁₂, sites that are vacant in the conventional garnet structure Li₃Ln₃Te₂O₁₂. Li₇La₃Zr₂O₁₂ in a cubic phase showed an ionic conductivity as high as 2.4 × 10⁻⁴ S cm⁻¹ at 22 °C⁴, but it

was achieved only in alumina crucibles. This conductivity was much higher than that of its parallel in tetragonal phase, which was 2.3 × 10⁻⁵ S cm⁻¹ at RT⁸. It was demonstrated that Al played an important role in stabilizing the highly conductive cubic phase, although the details of the stabilizing mechanism are still controversial^{9,10,11}. Some results showed that Al was rich in grain boundaries⁹, while other work demonstrated that Al could dope into the crystal structure and occupied tetrahedral 24*d* sites^{10,11}.

Up to now, aliovalent doping has been used as a strategy to increase the ionic conductivity of Li₇La₃Zr₂O₁₂. For example, the composition Li_{7-x}La₃Zr_{2-x}M_xO₁₂ (M = Ta, Nb)^{12,13} showed a higher ionic conductivity than the base material. Li_{6.5}La₃Zr_{1.5}Ta_{0.5}O₁₂, an analogue synthesized by hot pressing, exhibited an even higher ionic conductivity of 8.7 × 10⁻⁴ S cm⁻¹ at RT¹⁴. Moreover, Li_{7-2x}La₃Zr_{2-x}Te_xO₁₂ (*x* = 0.125, 0.25) managed a superior room temperature ionic conductivity of 1.02 × 10⁻³ S cm⁻¹ with *x* = 0.25, but no clear conducting mechanism has been reported yet¹⁵. In addition, the presence or lack of Al contamination in those compounds studied needs further clarification, since alumina crucibles were used in the calcination processes. If any Al existed in the compounds, its role in these high conductive electrolytes should be explained, in order to understand the co-doping of Al and Te and their synergistic effects on the enhanced ionic conductivities.

In this work, we systematically studied a series of different $\text{Li}_{7-2x-3y}\text{Al}_y\text{La}_3\text{Zr}_{2-x}\text{Te}_x\text{O}_{12}$ ($0 \leq x \leq 1$, $y = 0.25, 0.7$) solid solutions. Different techniques were used to study the synergistic effects of co-dopants Al and Te on stabilizing the crystal structure and enhancing the ionic conductivity. As well, the lithium transport mechanism in co-doped $\text{Li}_7\text{La}_3\text{Zr}_2\text{O}_{12}$ was examined and discussed.

Experimental

A conventional solid state reaction was used to synthesize the garnet-type electrolyte. The starting materials, $\text{LiOH} \cdot \text{H}_2\text{O}$, La_2O_3 , ZrO_2 and TeO_2 (purities of 95.0%, 99.99%, 99.0% and 99.99% respectively, all from the Sinopharm Chemical Reagent Co., Ltd), were mixed and ground by a planetary grinder, with isopropanol used as grinding reagent. The precursors were ground for 12 h and dried in a 120 °C box, then calcined at 800 °C for 12 h. After the second grinding and drying the material was pressed into pellets at 2 MPa by uniaxial cold pressing. Finally, the pellets with Te, covered with green constituent powder, were sintered at 1150 °C for 12 h in Al_2O_3 and ZrO_2 crucibles in order to get Al-containing and Al-free compositions respectively. In order to get a pure phase with cubic symmetry, the pellet with the composition of $\text{Li}_7\text{La}_3\text{Zr}_2\text{O}_{12}$ (*i.e.* without Te doping) was sintered at 1150 °C for 36 h in an alumina crucible.

X-ray powder diffraction (XRD) was used to characterize the crystal phases. A Panalytical X'Pert (Philip, Netherlands) instrument with Cu K α radiation was used for this purpose.

Elastic coherent neutron scattering experiments were performed on the high-resolution powder diffractometer SPODI at the research reactor FRM-II (Garching, Germany)¹⁶. Monochromatic neutrons ($\lambda = 1.5482$ Å) were obtained at a 155° take-off angle using the (551) reflection of a vertically focused composite Ge monochromator. The vertical position sensitive multidetector (300 mm effective height) used for data collection consisted of 80 ³He tubes and covered a 2 θ angular range of 160°. Measurements were performed in Debye–Scherrer geometry. Data was collected for 4 h from a powder sample in a thin-walled (0.15 mm) vanadium can, 13 mm in diameter. Refinement of the obtained neutron powder diffraction data was performed using the FullProf software package¹⁷. The peak profile shape was described by a pseudo-Voigt function. The background of the diffraction patterns was fitted using a linear interpolation between selected data points in nonoverlapping regions. The scale factor, lattice parameters, fractional coordinates of atoms and their iso-/anisotropic displacement parameters, angular shift, profile shape parameters and half width (Caglioti) parameters were allowed to vary during fitting.

The apparent density was measured using the weight and dimensions of pellets, and the relative density was calculated from the apparent and theoretical densities. A Hitachi S-4800 scanning electron microscope was used to check the cross-section morphology of samples.

AC impedance measurements were undertaken to measure conductivity, using a Solatron 1260 impedance analyzer with the frequency range of 1 to 10⁶ Hz and an amplitude of 100 mV. The measurement cell was constructed as follows: first, silver slurry was spread onto the surfaces of pellets and cured at 600 °C for 30 minutes in order to vaporize organic solvent. Next, the silver-

coated pellets were placed between two pieces of steel for testing. Test temperatures were varied from 50 to 150 °C at 10 °C intervals in order to study the temperature dependent relationship. The electronic conductivity was measured by the DC polarization method using a Solatron 1287 electrochemical analyzer with a polarization potential of 0.1 V. The holding time was 10,000 seconds.

Magic angle spinning nuclear magnetic resonance (MAS NMR) technique was used to probe the local chemical environment of the atoms and to analyze the lithium dynamics of the materials. The ⁶Li and ²⁷Al MAS NMR spectra were gathered at Larmor frequencies of 58.9 MHz and 104.3 MHz respectively on a Bruker Avance 400 NMR spectrometer with a sample spinning speed of 25 kHz. The chemical shifts of the ⁶Li and ²⁷Al were calibrated by using LiCl powder (0 ppm) and Al(OH)₃ (0 ppm) respectively. ²⁷Al MAS NMR spectra were collected using a small angle pulse of 1 μ s and a recycle delay of 0.1 s. ⁶Li MAS NMR spectra were collected using a 1/6.25 π pulse and a recycle delay of 40 s. The saturation recovery method was used here to characterize the spin lattice relaxation times for different lithium sites.

Results and discussion

In order to study the synergistic effects of Al and Te on the composition and phases of the garnet materials, a series of $\text{Li}_{7-2x}\text{La}_2\text{Zr}_{2-x}\text{Te}_x\text{O}_{12}$ ($0 \leq x \leq 1$) solid solutions were synthesized in alumina (Al_2O_3) and zirconium dioxide (ZrO_2) crucibles respectively. Fig. S1 (a) shows the XRD patterns of $\text{Li}_{7-x}\text{La}_3\text{Zr}_{2-x}\text{Te}_x\text{O}_{12}$ calcined in the alumina crucibles. These samples formed solid solutions with x ranging from 0 to 0.75 and the XRD data indicated a pure phase with cubic structure. However, for samples with $x = 1$, small amounts of La_2O_3 and $\text{La}_{0.5}\text{Zr}_{0.5}\text{O}_{1.75}$ were detected in addition to the cubic phase. Fig. S1 (b) shows the XRD patterns of $\text{Li}_{7-2x}\text{La}_2\text{Zr}_{2-x}\text{Te}_x\text{O}_{12}$ samples calcined in ZrO_2 crucibles. For $x = 0$, the main phase was tetrahedral with a small amount of $\text{La}_{0.5}\text{Zr}_{0.5}\text{O}_{1.75}$ impurity in the structure. However, for $x = 0.25$, the material was transformed into a cubic structure while a small amount of $\text{La}_{0.5}\text{Zr}_{0.5}\text{O}_{1.75}$ impurity retained. With $x = 0.5$ and 0.75, a pure phase with cubic structure could be obtained. Finally, the composition with $x = 1$ exhibited the same behavior

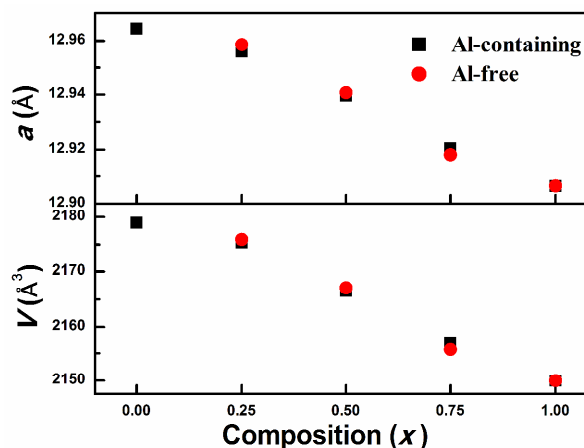


Fig. 1 Composition dependent lattice parameters of $\text{Li}_{7-x}\text{La}_3\text{Zr}_{2-x}\text{Te}_x\text{O}_{12}$ ($0 \leq x \leq 1$) solid solutions (with and without Al).

as its parallel sintered in the alumina crucible. It was apparent that Al played an important role in the formation of phase-pure materials by stabilizing the crystal structure and/or promoting the formation of a solid solution of garnet materials, as for some compositions ($x = 0, 0.25$), no phase-pure samples could be obtained without Al. In addition, in all of the cubic phase samples obtained, the crystal lattice parameter a decreased as the Te content increased (Fig. 1). This behavior was due to a difference in the ionic radii of Te^{6+} ions (0.56 Å) and Zr^{4+} ions (0.72 Å) while 6-coordinated. The linear changing of lattice parameters without any phase transformations confirmed the formation of garnet structure solid solutions with the addition of Te.

It is well-known¹⁴ that the conventional garnet structure, $\text{A}_3\text{B}_2\text{C}_3\text{O}_{12}$, has A, B and C occupying 24c sites, 16a sites and 24d sites, respectively. For a lithium ion conductor, C represents lithium. In $\text{Li}_3\text{La}_3\text{Nb}_2\text{O}_{12}$ or $\text{Li}_7\text{La}_3\text{Zr}_2\text{O}_{12}$ analogues, some lithium ions occupy the conventional tetrahedral 24d sites (Li1) while others take up distorted octahedral 96h sites (Li2) which are empty in the conventional garnet structure, while the other atoms (La, Zr/Nb and O) occupy their conventional sites^{18,19} (Fig. S2).

In a doped system, it is necessary to check the local structure of these newly-formed materials to find out what sites the doped atoms are occupying. Here, different techniques such as solid state NMR and EDS analysis were used in order to understand the co-doping effects of Al and Te.

Fig. 2 shows the ^{27}Al NMR spectra of samples sintered in alumina crucibles and with different amounts of Te. The observed chemical shift of the ^{27}Al peak was around +64 ppm, indicating that Al was tetrahedrally coordinated in the cubic garnet structure and located at the Li1 sites^{10,11}. No extra peak could be observed in the ^{27}Al spectra, implying that the substitution of Zr and/or La was not occurring¹⁰. The relatively minor occupancy of Al was more likely to happen at the 24d sites of Li1 atoms. Taking into account these findings, the chemical formula of the Al-containing solid solutions could thus be written as $\text{Li}_{7-2x-3y}\text{Al}_y\text{La}_3\text{Zr}_{2-x}\text{Te}_x\text{O}_{12}$. In addition, the integrated area of the ^{27}Al peak decreased with Te content, and vanished after the Te content reached about 0.5, indicating that there was no aluminum existing in the samples with $x \geq 0.5$.

EDS analysis was also carried out to detect the content of

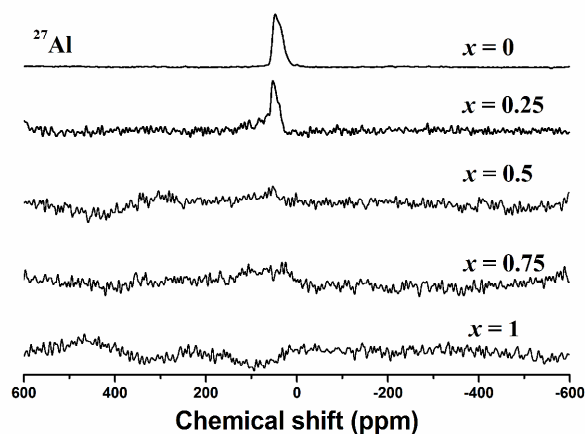


Fig. 2 ^{27}Al MAS NMR spectra of the $\text{Li}_{7-x}\text{La}_3\text{Zr}_{2-x}\text{Te}_x\text{O}_{12}$ ($0 \leq x \leq 1$) solid solutions sintered in Al_2O_3 crucibles.

aluminum in the samples calcined in Al_2O_3 crucibles, with the results showing that for $x = 0$ and 0.25, the $\text{Li}_{7-2x-3y}\text{Al}_y\text{La}_3\text{Zr}_{2-x}\text{Te}_x\text{O}_{12}$ material yielded $y = 0.26$ and 0.07 respectively. For $x \geq 0.5$, Al could not be detected, which was in agreement with the above NMR results. Considering the crystal structure and the composition of the solid solutions, it seemed that both Al and Te could stabilize the cubic phase, with Al occupying 24d sites and Te 16a sites. Here, the substitution of Zr with Te at 16a sites was easier than the doping of Al at 24d sites given the experimental conditions. For the $x = 0$ and $x = 0.25$ samples, the Te content was not sufficient to stabilize the cubic phase. Consequently, the cubic structure collapsed into the tetragonal phase and $\text{La}_{0.5}\text{Zr}_{0.5}\text{O}_{1.75}$ impurity containing cubic phase respectively, as the samples were sintered in ZrO_2 crucibles. In contrast, when the samples were sintered in alumina crucibles, they reacted with the crucibles and Al atoms entered into the crystal structure, with the co-doping of Al and Te sustaining the pure cubic phase. For $x = 0.5$ and 0.75, the Te content was sufficient to stabilize the cubic phase by itself and furthermore restrained the reaction of samples with alumina crucibles. The lack of an Al signal in ^{27}Al MAS NMR and EDS analysis indicated that Al atoms did not exist in these compositions. The lattice parameters of these samples with and without Al also showed the same trend, with negligible differences (Fig. 1). It is of note that when the pristine $\text{Li}_7\text{La}_3\text{Zr}_2\text{O}_{12}$ was sintered in alumina crucibles for just 12 h, the sample showed a tetragonal structure, as it needed more sintering time to allow enough Al atoms to dope into the crystal structure to show a cubic phase.

The model proposed by Awaka *et al.*²⁰ was used for the Rietveld refinement of the Al-containing pristine $\text{Li}_{7-x}\text{La}_3\text{Zr}_{2-x}\text{Te}_x\text{O}_{12}$ structure (for $x = 0, 0.25$) and Al-free sample with $x = 0.25$. For the samples with $x = 0.25$, the Te atoms were considered to be occupying Zr (16a) sites due to the close values of their ionic radii. The occupancies of La, Zr/Te, and O were fixed to be 3, 2 and 12 atoms per formula unit respectively. However, the presence of relatively heavy La and Zr atoms in the structure complicated refinement of the “light” aluminum and lithium atoms. Furthermore, the neutron scattering length for Al

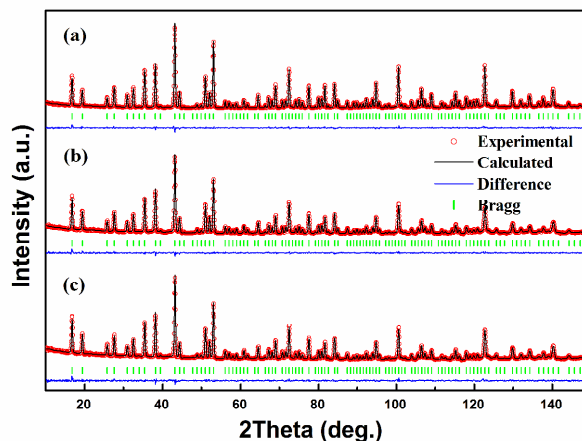


Fig. 3 Rietveld refinement of the structure models, based on neutron powder diffraction data of $\text{Li}_{7-x}\text{La}_3\text{Zr}_{2-x}\text{Te}_x\text{O}_{12}$ for Al-containing samples with (a) $x = 0$, (b) $x = 0.25$, and (c) Al-free samples with $x = 0.25$ at room temperature.

Table 1 Refined structural parameters of $\text{Li}_{7-x}\text{La}_3\text{Zr}_{2-x}\text{Te}_x\text{O}_{12}$ (Space group $Ia-3d$, No.230). Displacement parameters for Li were modeled in isotropic approximation. Numbers in parentheses give statistical deviations for the last significant 5 digits. Fit residuals (not corrected for background) R_p , R_{wp} and χ^2 correspond to profile, weighted profile residuals and goodness of fit, respectively.

| | $x = 0$, Al-containing | $x = 0.25$, Al-containing | $x = 0.25$, Al-free |
|------------------------------|----------------------------|-------------------------------|-------------------------|
| a (Å) | 12.96473(7) | 12.96183(12) | 12.96251(12) |
| R_p , % | 2.58 | 2.26 | 2.28 |
| R_{wp} , % | 3.34 | 2.85 | 2.91 |
| χ^2 | 1.56 | 1.18 | 1.18 |
| Li 24 <i>d</i> | 42.4(8) | 52.4(12) | 56.8(12) |
| occ. (%) / f.u. | /1.27(2) | /1.57(4) | /1.70(3) |
| Al 24 <i>d</i> * | 8.4/0.26 | 2.4/0.072 | 0/0 |
| occ. (%) / f.u. ^a | | | |
| Li 96 <i>h</i> | 41.5(2) | 39.3(3) | 40.6(3) |
| occ. (%) / f.u. | /4.98(2) | /4.72(4) | /4.87(4) |
| Li/Al (24 <i>d</i>) | 3.1(3) | 2.5(2) | 3.4(2) |
| B_{iso} (Å ²) | | | |
| Li (96 <i>h</i>) | 2.0(1) | 2.4(2) | 2.6(2) |
| B_{iso} (Å ²) | | | |

* The Al content was taken from EDS analysis.

is rather low and a small concentration in the compound is 10 difficult to quantify using neutron powder diffraction. Therefore, the amount of Al in the samples was taken from the EDS analysis and fixed at 0.26 and 0.07 for Al-containing samples with $x = 0$ and 0.25. The location of aluminum in lithium sites with 24*d* symmetry was selected as it showed the best fitting as well as 15 being in agreement with our study and the recent investigations of Buschmann *et al.*, where this model was confirmed by NMR analysis¹¹. The total Li amount was fixed at formula stoichiometry values while considering the presence of Al: 6.25

and 6.29 for Al-containing samples with $x = 0$ and 0.25 20 respectively, and 6.5 for the Al-free sample with $x = 0.25$. The best fits of neutron diffraction data were obtained with the parameters listed in Table 1 and the results of Rietveld refinement are shown in Fig. 3.

The anomalously large isotropic displacement parameters of 25 lithium in 24*d* and 96*h* sites could be attributed to static lithium disorder, which is likely the reason for the typical high Li ion mobility in garnet-like structures. The occupancy of lithium in the 24*d* sites ranged from 42.4 to 56.8%, and in 96*h* sites it was about 40%. Such findings were in a good agreement with the literature 30 for room temperature NPD analysis of Al-containing $\text{Li}_7\text{La}_3\text{Zr}_2\text{O}_{12}$ material¹¹.

Fig. 4 shows the cross sections of the Al-containing and Al-free samples. The grain size of samples increased alongside the Te content until x reached 0.75. At $x = 1$, the samples exhibited 35 mixed phases for Al-containing and Al-free compositions, which might have affected the crystallization and grain size. The substitution of Te atoms contributed to the growth of grains and the percentage of grain boundaries decreased with Te content, a trend which should have had a positive effect on ionic 40 conductivity. Furthermore, there was significant porosity in the samples with $x = 0$ and 0.25 while the packing of grains became better with increasing Te content, which suggested that the samples with higher x values had higher relative densities and better grain boundaries.

Fig. 4 (k) gives the EDS analysis of the sample of $x = 0.25$ 45 synthesized in an Al_2O_3 crucible. The Al, La, Zr, Te, and O were distributed homogeneously across the cross-sections, with no evidence that Al was enriched in grain boundaries.

The density of a sample and its amount of grain boundaries 50 play an important role in determining mechanical strength and ionic conductivity. Table 2 shows the relative densities of samples with and without the presence of aluminum. The relative density of the samples rose along with Te content, which was in agreement with the information gleaned from SEM. However, the

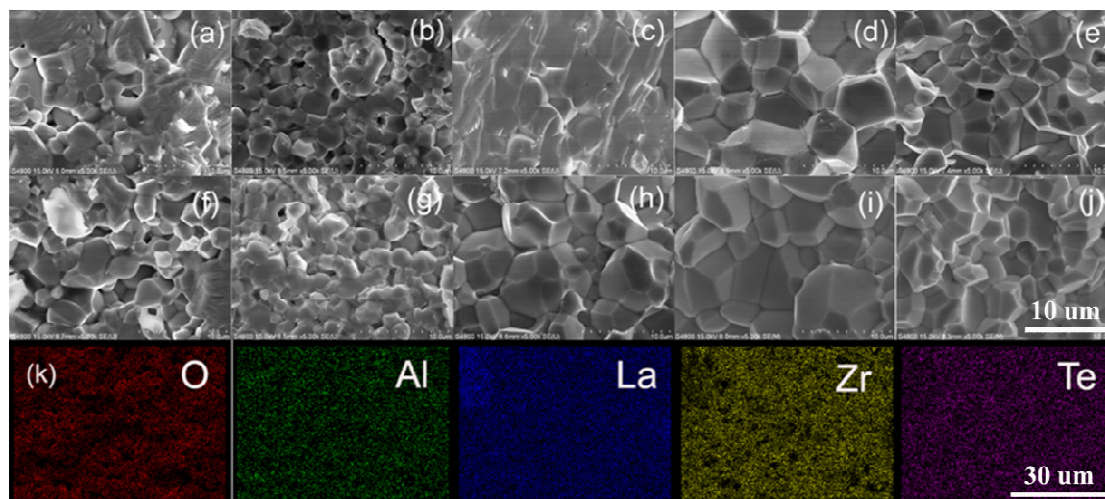


Fig. 4 Cross section morphology of $\text{Li}_{7-x}\text{La}_3\text{Zr}_{2-x}\text{Te}_x\text{O}_{12}$ ($0 \leq x \leq 1$) solid solutions with and without Al. (a) $x = 0$, (b) $x = 0.25$, (c) $x = 0.5$, (d) $x = 0.75$, (e) $x = 1$ with Al; (f) $x = 0$, (g) $x = 0.25$, (h) $x = 0.5$, (i) $x = 0.75$, (j) $x = 1$ without Al. (k) EDS analysis of the Al-containing 60 sample with composition $x = 0.25$. Different colors represent the different elemental distributions across the sample: red – O, dark green – Al, blue – La, yellow-green – Zr, purple – Te.

Table 2 Properties of $\text{Li}_{7-2x}\text{La}_2\text{Zr}_{2-x}\text{Te}_x\text{O}_{12}$ ($0 \leq x \leq 1$) solid solutions sintered in Al_2O_3 and ZrO_2 crucibles.

| Composition (x) | Relative density | | Activation energy (eV) | | Conductivity/RT $\times 10^{-5} \text{ S cm}^{-1}$ | | dc-conductivity/RT $\times 10^{-8} \text{ S cm}^{-1}$ | |
|-----------------|-------------------------|----------------|---------------------------------------|---------------------------------------|--|----------------|---|----------------|
| | Al_2O_3 | ZrO_2 | Al_2O_3 | ZrO_2 | Al_2O_3 | ZrO_2 | Al_2O_3 | ZrO_2 |
| 0.00 | 0.800 | --- | 0.41 ¹ / --- | --- | 1.3 | --- | --- | --- |
| 0.25 | 0.824 | 0.802 | 0.33 ¹ / 0.46 ² | 0.37 ¹ / 0.47 ² | 40.0 | 36.9 | 2.53 | 0.05 |
| 0.5 | 0.875 | 0.869 | 0.37 ¹ / 0.48 ² | 0.39 ¹ / 0.47 ² | 21.9 | 23.0 | 1.72 | 0.82 |
| 0.75 | 0.882 | 0.862 | 0.45 ¹ / 0.49 ² | 0.44 ¹ / 0.48 ² | 9.47 | 8.2 | 0.56 | 2.53 |
| 1 | 0.860 | 0.866 | 0.43 ¹ / 0.48 ² | 0.42 ¹ / 0.49 ² | 4.6 | 6.3 | 1.48 | 0.24 |

1. The activation energies were calculated in the temperature range of 150 °C ~ RT,

2. The activation energies were calculated in the temperature range of RT ~ -50 °C.

relative densities of the samples were still less than 90%, and were even lower, at around 80%, for samples with $x = 0$ and 0.25. These low relative densities were detrimental to the mechanical strength and ionic conductivities of the samples and were likely due to the uniaxial cold pressing or the sintering method used.

Fig. 5 shows Nyquist plots of the Al-containing sample with $x = 0.25$. There was a semicircle at the high frequency side and a dispersive line at the low frequency side, which represented the total resistance and electrode process, respectively (Fig. 5 (a), (b)).

It was believed that the dispersive line at the low frequency side could be attributed to the Li-Ag alloy process since Ag electrodes were used, so lithium electrodes were also selected in order to give evidence for this hypothesis. A semicircle attributed to the lithium electrode duly appeared in the same frequency region (Fig. 5 (c)). Meanwhile, the high frequency semicircle decreased

and vanished with increasing test temperature, leaving just a dispersive line at the low frequency side (Fig. 5 (a), (b)). This behavior was due to the decrease in characteristic time with increasing test temperature and Li^+ mobility, and the characteristic time exceeded the frequency window of the

experiment at higher temperatures. Since it was not possible to distinguish the bulk conductivity and grain boundary conductivity from the Nyquist plots, total conductivity was used here. The inductive effect due to conductive wires was also considered in the experiment, and $L(R1CPE1)(R2CPE2)$ and $LR1(R2CPE2)$

equivalent circuits were used to fit the Nyquist plots at low and high temperatures, respectively. In these models, R1 represents the total resistance of the sample and R2 represents the Li-Ag alloy process. Because of the complexity of the electrode process, the fitting was performed in the limited frequency range instead

of the full frequency range. The fitting results are shown in Table S1. It was worth noting that the CPE1 was at the level of 10^{-10} F , which is a characteristic value for bulk materials. Thus, the contribution of grain boundary conductivity to the total was quite small or even negligible, implying that the bulk contributed

almost all the total conductivity. The temperature dependent ionic conductivities are shown in Fig. 6 and fit the Arrhenius plots well in both high and low temperature ranges. There was a distinctive change of slope at around RT, and the activation energies were higher in the low temperature side than that in the high

temperature side. This might have been due to the ion trapping effect, which is common in crystals with defects^{21,22}. Here, discussion was based on the activation energies calculated in the high temperature range. The Te doped samples showed a much higher ionic conductivity compared to the pristine material, with

detailed data listed in Table 2. Samples with $x = 0.25$ exhibited the highest room temperature ionic conductivity, $\sigma_{\text{rt}} = 4 \times 10^{-4} \text{ S cm}^{-1}$, and the lowest activation energy, $E_a = 0.33 \text{ eV}$. Surprisingly,

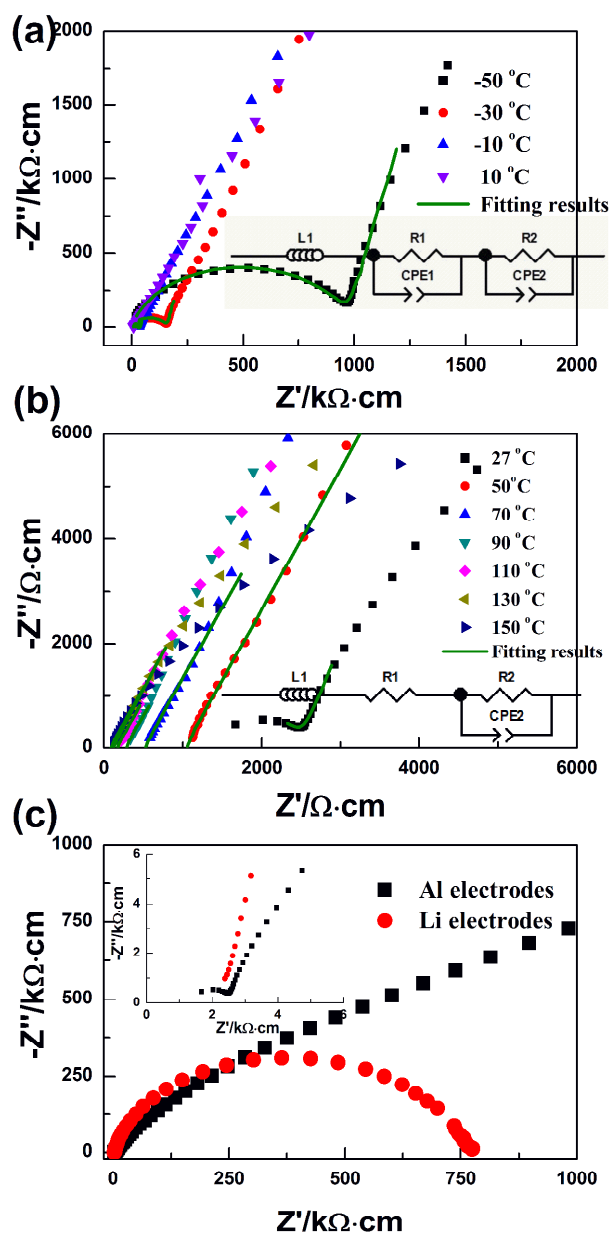


Fig. 5 (a), (b) Nyquist plots of the Al-containing sample with composition $x = 0.25$ measured at different temperatures, with the fitting results of data shown as green solid lines. (c) Nyquist plots of Al-containing samples with composition $x = 0.25$ at room temperature, with different electrodes used. The inlet was the amplification of this Nyquist plot at the high frequency side.

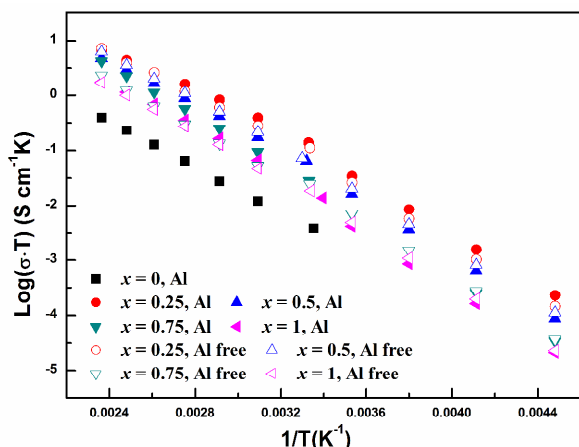


Fig. 6 Arrhenius plots of $\text{Li}_{7-x}\text{La}_3\text{Zr}_{2-x}\text{Te}_x\text{O}_{12}$ ($0 \leq x \leq 1$) solid solutions with and without Al.

ionic conductivities actually decreased with Te content, partially owing to the fact that activation energies increased. From SEM results and the increase in measured relative density, it was anticipated that the amount of grain boundaries would decrease and that the ionic conductivity of the grain boundary component would increase with more Te doping (although its effect was quite small, from the above discussion). This left structural factors (bulk conductivity) as the sole reason for the overall decrease in total conductivity and rise in activation energy. One explanation was likely the shrinking of the crystal lattice, which would narrow the bottleneck in the lithium jump path of the bulk crystal. The composition with $x = 0.25$ showed the highest ionic conductivity which was probably due to it having both the lowest activation energy and the optimum lithium content, with 6.5 formula parts per unit. This number agreed well with the literature^{12,13,14,23}. Of the two samples with $x = 0.25$, the one without Al yielded a slightly lower room temperature ionic conductivity and higher activation energy, likely because of the existence of $\text{La}_{0.5}\text{Zr}_{0.5}\text{O}_{12}$ impurity, which would affect the bulk composition (and bulk conductivity) and/or block lithium transport through grain boundaries. For the Te-doped samples with $x \geq 0.5$, whether they were sintered in alumina or zirconium dioxide crucibles made little difference for their ionic conductivities and activation energies, which agreed with the crystal structure analysis from XRD and composition results.

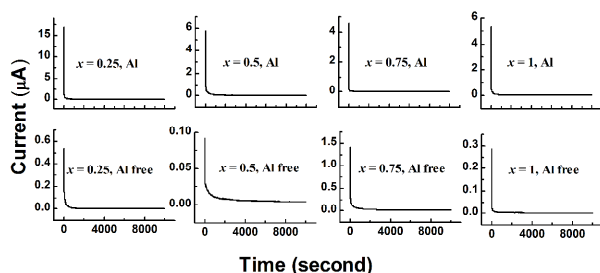


Fig. 7 DC polarization of $\text{Li}_{7-x}\text{La}_3\text{Zr}_{2-x}\text{Te}_x\text{O}_{12}$ ($0 \leq x \leq 1$) samples with and without Al. The different current drops of samples were due to the difference in electrode processes, which affected the initial current. The current asymptote was determined by the electronic resistance of the bulk sample.

An ideal solid electrolyte must be solely an ionic (*i.e.*, not an electronic) conductor in case there is a short circuit in the lithium ion battery. The DC polarization method was used to measure the electronic conductivity of samples (Fig. 7). These electronic conductivities were on the order of $10^{-8} \text{ S cm}^{-1}$, much lower than the ionic conductivities of the samples ($\sim 10^{-4} \text{ S cm}^{-1}$) (Table 2). Thus, the transference number of lithium ions t_{Li^+} for the garnets here was nearly unity, which indicated that the co-doped garnets were purely lithium ion conductors. The cyclic voltammetry method was used to gather more information on the electrochemical stability of the co-doped samples. There was no oxidation or reduction peak except from the Li-Ag alloy and de-alloy processes in the range of $-1 \sim 9 \text{ V}$ (for the sake of concision, the cyclic voltammetry plot is not given here). Thus the co-doped samples were suitable for lithium ion batteries.

To understand the Li^+ conducting mechanism in the co-doped garnet structure, it is necessary to differentiate the two Li sites, tetrahedral $24d$ sites and distorted octahedral $96h$ sites, and to understand the Li^+ environmental and local structural changes when two doping atoms are co-doped into the garnet structure.

Solid state NMR techniques, *esp.* magic angle spinning, are useful tools for differentiating these Li sites. Fig. 8 shows ^6Li MAS NMR spectra, where the two lithium peaks were successfully differentiated by fitting with two Lorentzian peaks, except for samples with $x = 1$ where an additional peak was required for a quality fit. However, the attribution of the third peak was not clear and it also overlapped with the first two peaks, possibly impacting their accuracy. Therefore, the fitting results for $x = 1$ were used just as a reference. All parameters yielded from the fitting process are listed in Table 3 and Table 4. As was done with neutron diffraction data, the total number of lithium ions was set using the stoichiometry of the solid solution formula. The integrated area of each NMR peak was used to calculate the number of lithium ions that occupied their corresponding sites. It was found that the low field side peak at around 1.9 ppm represented about 90% of the total integrated area, and more than 3 lithium ions per formula unit (f.u.) at this site was observed for nearly all samples. This peak was assigned to Li2 sites, as the number of lithium ions occupying Li1 sites cannot exceed 3 in the garnet structure. This left the peak at the high field side to be assigned to Li1 sites. The occupation of the Li1 and Li2 sites in all the samples was found to be less than 0.5, with Li2 sites showing consistently higher occupation values. The occupation value also generally decreased with increases in the Te content. The lack of occupancy in Li1 sites and higher occupancy in Li2 sites might have been the reason of the high ionic conductivity of this garnet-type material. However, this result was not in agreement with the literature²⁴, where the occupancy of Li1 sites increased while that of Li2 sites decreased with a decrease in the total lithium amount. For samples with $x = 0.25$, the occupancy of Li1 sites in Al-containing samples was much lower than that of Al-free samples, suggesting that Al took up Li1 sites. The difference in the calculated Li occupancy at their corresponding sites from neutron diffraction and ^6Li NMR results might be due to the quadrupole effects of Al at Li1 sites.

When the line shape is dominated by motional narrowing (MN), the line width of the lithium peak is usually used to describe the lithium mobility²⁵. A lithium peak with a narrow line

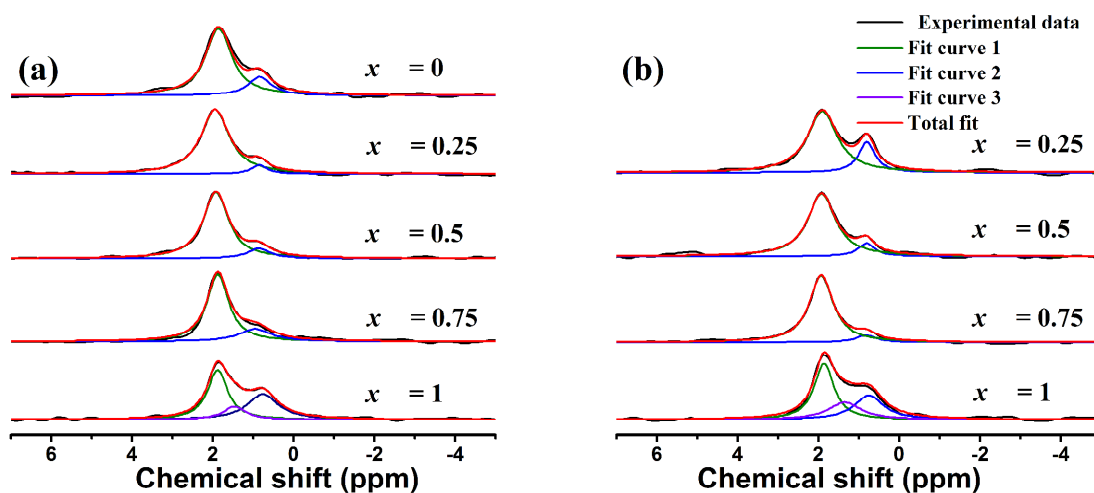


Fig. 8 ${}^6\text{Li}$ MAS NMR spectra of the (a) Al-containing and (b) Al-free $\text{Li}_{7-x}\text{La}_3\text{Zr}_{2-x}\text{Te}_x\text{O}_{12}$ ($0 \leq x \leq 1$) samples. The black line represents experimental data, the green fit curve corresponds to Li2 sites, the blue fit curve represents Li1 sites, and the red curve is the total fit.

Table 3 Fitting results of ${}^6\text{Li}$ MAS NMR spectra of $\text{Li}_{7-2x}\text{La}_2\text{Zr}_{2-x}\text{Te}_x\text{O}_{12}$ ($0 \leq x \leq 1$) solid solutions with Al doping.

| x | Fit peak 1 (Li1) | | | | | | Fit peak 2 (Li2) | | | | |
|------|------------------|----------|---------|-------|------|-------------|------------------|---------|------|------|--|
| | Center(ppm) | FWHM(Hz) | Area(%) | f.u. | Occ. | Center(ppm) | FWHM(Hz) | Area(%) | f.u. | Occ. | |
| 0 | 0.790 | 35.63 | 15.73 | 0.98 | 0.33 | 1.850 | 49.29 | 84.27 | 5.27 | 0.44 | |
| 0.25 | 0.860 | 33.33 | 8.68 | 0.54 | 0.18 | 1.947 | 48.47 | 91.32 | 5.74 | 0.48 | |
| 0.5 | 0.865 | 41.46 | 12.16 | 0.73 | 0.24 | 1.924 | 42.93 | 87.84 | 5.27 | 0.44 | |
| 0.75 | 0.883 | 44.11 | 14.68 | 0.81 | 0.27 | 1.867 | 37.13 | 85.32 | 4.69 | 0.39 | |
| 1 | 0.747 | 48.17 | 33.46 | 1.673 | 0.56 | 1.873 | 35.22 | 50.91 | 2.55 | 0.21 | |

$x=1$, Fit peak 3: 1.394, 40.05, 15.63.

Table 4 Fitting results of ${}^6\text{Li}$ MAS NMR spectra of $\text{Li}_{7-2x}\text{La}_2\text{Zr}_{2-x}\text{Te}_x\text{O}_{12}$ ($0 < x \leq 1$) solid solutions without Al doping.

| x | Fit peak 1 (Li1) | | | | | | Fit peak 2 (Li2) | | | | |
|------|------------------|----------|---------|------|------|-------------|------------------|---------|------|------|--|
| | Center(ppm) | FWHM(Hz) | Area(%) | f.u. | Occ. | Center(ppm) | FWHM(Hz) | Area(%) | f.u. | Occ. | |
| 0.25 | 0.800 | 29.21 | 21.88 | 1.42 | 0.47 | 1.90 | 52.29 | 78.12 | 5.08 | 0.42 | |
| 0.5 | 0.809 | 29.56 | 10.85 | 0.65 | 0.22 | 1.911 | 48.53 | 89.15 | 5.79 | 0.48 | |
| 0.75 | 0.813 | 36.51 | 8.66 | 0.48 | 0.16 | 1.929 | 41.52 | 91.34 | 5.02 | 0.42 | |
| 1 | 0.770 | 47.11 | 27.62 | 1.38 | 0.46 | 1.864 | 31.51 | 42.93 | 2.15 | 0.18 | |

$x=1$, fit peak 3: 1.413, 58.89, 29.44.

width indicates a high jump rate and good lithium mobility, while the opposite applies for a wide line width.

Here, the line width of the lithium peak ranged from 30–50 Hz with MAS. It was believed that the change in line width was associated with the translational motion of lithium in the structure, which was responsible for the ionic conductivity. For Al-containing samples, the full width at half maximum (FWHM) of the Li1 peak showed the smallest value (33.33 Hz) for compositions with $x = 0.25$. FWHM increased with Te content, indicating a decrease in lithium mobility. This correlated well with the trend of ionic conductivity calculated from AC impedance. However, the FWHM of the Li2 peak decreased with Te content, indicating an increase of lithium mobility for the Li-ions located at this site, which was contrary to the trend of ionic conductivity observed. Therefore, from these results, we propose that the mobility at Li1 sites was the determining factor for the ionic conductivity of the cubic garnet structure. This observation is in agreement with the $24d$ - $96h$ - $48g$ - $96h$ - $24d$ lithium transport loop proposed by Akawa *et al.*, where Li1 ($24d$) sites were the connection points of this path and believed to determine the lithium diffusion kinetics²⁰. There is disagreement in the literature

about this point, as, Wullen *et al.*²⁶ concluded from solid state NMR data that lithium bypassed Li1 sites, *i.e.* lithium ions simply jumped from one Li2 site to a neighboring Li2 site in $\text{Li}_5\text{La}_3\text{Nb}_2\text{O}_{12}$. They successfully separated Li1 and Li2 sites with ${}^6\text{Li}$ NMR and found that there was no exchange between these two sites, which was the evidence of their transport mechanism. However, a relaxation delay of 7200 s was needed to differentiate the two lithium peaks in their experiment, indicating a very long spin lattice relaxation time and negligible mobility for Li1.

The spin lattice relaxation time (T_1) of lithium at different sites was characterized by the saturation recovery method (Fig. 9). For the Al-containing composition with $x = 0.25$, the T_1 of Li1 was 19.43 s and about 2.39 s for Li2, indicating that Li2 sites showed a higher jump rate than Li1 sites. For the Al-containing composition with $x = 0.5$, the T_1 of Li1 was 34.26 s and about 0.81 s for Li2. Sites with the lowest jump rate (here Li1) determine the whole jump rate along the transport path. Additionally, the Li1 spin relaxation time of 19.43 s was much smaller than that in the $\text{Li}_5\text{La}_3\text{Nb}_2\text{O}_{12}$ analogue²⁶, but not much larger than the T_1 of Li2 in the co-doped $\text{Li}_7\text{La}_3\text{Zr}_2\text{O}_{12}$ analogue. Thus, from a dynamic point of view, it was believed to be

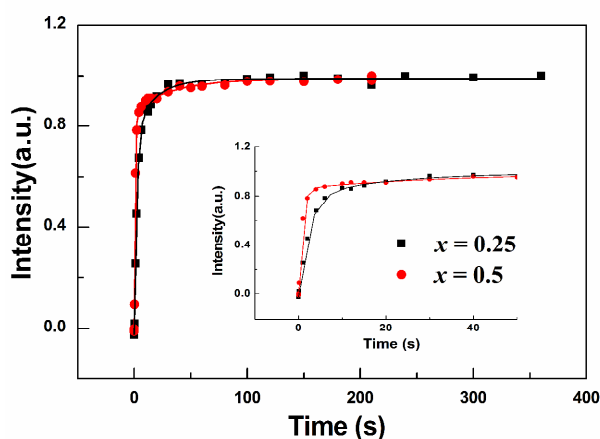


Fig. 9 ^6Li saturation recovery time (T_1) experiments.

possible to form a successive jump route through Li1 and Li2 sites in $\text{Li}_{7-2x}\text{La}_2\text{Zr}_{2-x}\text{Te}_x\text{O}_{12}$ and/or $\text{Li}_{7-2x-3y}\text{Al}_y\text{La}_3\text{Zr}_{2-x}\text{Te}_x\text{O}_{12}$ analogues, which was not possible in $\text{Li}_5\text{La}_3\text{Nb}_2\text{O}_{12}$. The complete replacement of Nb by Zr not only adjusted the lithium concentration, but also resulted in a change in the Li path bottleneck and environment in the garnet structure, which modified the lithium transport mechanism. From our results, the lithium environment and local structure in $\text{Li}_7\text{La}_3\text{Zr}_2\text{O}_{12}$ was not greatly changed by the partial replacement of Li by Al and Zr by Te, with the consequence that the original lithium transport mechanism remained²⁰.

To summarize, characterized by different methods at different size scales and at different time scales, the total ionic conductivity of samples was shown to be governed by the bulk structure, and the lithium transport along the jump route of the crystal structure was mainly determined by the Li mobility of Li1 sites. High resolution ^6Li MAS NMR successfully separated the lithium peak into two different peaks, Li1 and Li2, which made the study of lithium mobility at different sites possible. Temperature dependent ^6Li MAS NMR spectra would be collected in the future in order to further understand these dynamic properties of Li1 and Li2 sites.

Conclusions

Solid solutions of $\text{Li}_{7-2x}\text{La}_2\text{Zr}_{2-x}\text{Te}_x\text{O}_{12}$ ($0 \leq x \leq 1$) with and without Al doping were synthesized and investigated systematically. The sample with $x = 0.25$ showed the highest ionic conductivity, $\sigma_{\text{it}} = 4 \times 10^{-4} \text{ S cm}^{-1}$, and lowest activation energy, 0.33 eV, with an aluminum content of 0.07 mol per formula unit. The same composition without Al showed a slightly lower ionic conductivity due to the existence of an impurity phase. It was found that the doping of Al atoms occurred at 24d sites while Te occupied 16a sites. When $x = 0$ and 0.25, Al and Te codopants stabilized the cubic garnet structure. However, the occupancy of Te at 16a sites tended to depress the doping of Al into 24d sites. When x reached 0.5, Te was shown to stabilize the cubic structure on its own and restrained the reaction of samples with the alumina crucibles. Finally, the jump rate at Li1 sites was demonstrated to determine the bulk and total ionic conductivities. We concur with previous hypotheses of a lithium jump process

along the 24d-96h-48g-96h-24d route, with 24d sites being the key point in the path. As the understanding of garnet-type solid electrolyte increases, its promise in solving important issues with commercial lithium ion batteries will grow.

Acknowledgement:

Financial support from the National Basic Research Program of China (973 program, Grant No. 2011CB935903) and the National Natural Science Foundation of China (Grants No. 21233004 and 21021002) are gratefully acknowledged.

Notes and references

- ^a State Key Lab of Physical Chemistry of Solid Surface and Department of Chemistry, Xiamen University, Xiamen, 361005, China.
- ^b Heinz Maier-Leibnitz Zentrum (MLZ), Technische Universität München, Lichtenbergstr. 1, D-85748 Garching, Germany.
- ^c Department of Material Science and Engineering, Xiamen University, Xiamen, 361005, China.
- ^d National High Magnetic Field Laboratory, 1800 E. Paul Dirac Drive, Tallahassee, Florida, 32310, USA.
- 1 N. Kamaya, K. Homma, Y. Yamakawa, M. Hirayama, R. Kanno, M. Yonemura, T. Kamiyama, Y. Kato, S. Hama, K. Kawamoto and A. Mitsui, *Nat. Mater.*, 2011, **10**, 682.
- 2 M. Nagao, Y. Imade, H. Narisawa, T. Kobayashi, R. Watanabe, T. Yokoi, T. Tatsumi, R. Kanno, *J. Power Sources*, 2013, **222**, 273.
- 3 V. Thangadurai, H. Kaack and W. Weppner, *J. Am. Ceram. Soc.*, 2003, **86**(3), 437.
- 4 R. Murugan, V. Thangadurai and W. Weppner, *Angew. Chem. Int. Ed.*, 2007, **46**, 7778.
- 5 P. Birke, S. Scharner, R. A. Huggins, W. Weppner, *J. Electrochem. Soc.*, 1997, **144**, L167.
- 6 Y. W. Hu, I. D. Raistrick, R. A. Huggins, *J. Electrochem. Soc.*, 1977, **124**, 1240.
- 7 M. P. O'Callaghan, D. R. Lynham, E. J. Cussen and G. Z. Chen, *Chem. Mater.*, 2006, **18**, 4681.
- 8 J. Wolfenstine, E. Rangasamy, J. L. Allen, J. Sakamoto, *J. Power Sources*, 2012, **208**, 193.
- 9 Y. Q. Li, Z. Wang, C. L. Li, Y. Cao, X. X. Guo, *J. Power Sources*, 2014, **248**, 642.
- 10 A. Duvel, A. Kuhn, L. Robben, M. Wilkening and P. Heitjans, *J. Phys. Chem. C*, 2012, **116**, 15192.
- 11 H. Buschmann, J. Dolle, S. Berendts, A. Kuhn, P. Bottke, M. Wilkening, P. Heitjans, A. Senyshyn, H. Ehrenberg, A. Lotnyk, V. Duppel, L. Kienle and J. Janek, *Phys. Chem. Chem. Phys.*, 2011, **13**, 19378.
- 12 Y. T. Li, J. T. Han, C. A. Wang, H. Xie and J. B. Goodenough, *J. Mater. Chem.*, 2012, **22**, 15357.
- 13 S. Ohta, T. Kobayashi, T. Asaoka, *J. Power Sources*, 2011, **196**, 3342.
- 14 J. L. Allen, J. Wolfenstine, E. Rangasamy, J. Sakamoto, *J. Power Sources*, 2012, **206**, 315.
- 15 C. Deviannaproani, L. Dhivya, S. Ramakumar, R. Murugan, *J. Power Sources*, 2013, **240**, 18.
- 16 M. Hoelzel, A. Senyshyn, N. Juenke, H. Boysen, W. Schmahl, H. Fuess, *Nucl. Instrum. Methods Phys. Res. A*, 2012, **667**, 32.
- 17 J. Rodriguez-Carvajal, *Comm. Powder Diffr. Newsl.*, 2001, **26**, 12.
- 18 L. Truong, M. Howard, O. Clemens, K. S. Knight, P. R. Slater and V. Thangadurai, *J. Mater. Chem. A*, 2013, **1**, 13469.
- 19 V. Thangadurai, S. Narayanan, D. Pinzaru, *Chem. Soc. Rev.*, 2014, **43**, 4714.
- 20 J. Awaka, A. Takashima, K. Kataoka, N. Kijima, Y. Idemoto and J. Akimoto, *Chem. Lett.*, 2011, **40**, 60.
- 21 P. G. Bruce and A. R. West, *J. Solid State Chem.*, 1984, **53**, 430.
- 22 J. Percival, E. Kendrick, P. R. Slater, *Solid State Ionics*, 2008, 179, 1666.
- 23 H. Xie, J. A. Alonso, Y. T. Li, M. T. Fernandez-Diaz and J. B. Goodenough, *Chem. Mater.*, 2011, **23**, 3587.

-
- 24 E. J. Cussen, *J. Mater. Chem.*, 2010, **20**, 5167.
- 25 A. Kuhn, S. Narayanan, L. Spencer, G. Goward, V. Thangadurai, M. Wilkening, *Phys. Rev. B*, 2011, **83**, 094302.
- 26 L. V. Wullen, T. Echelmeyer, H. W. Meyer and D. Wilmer, *Phys. Chem. Chem. Phys.*, 2007, **9**, 3298.